energies

MDPI

Article

Experimental Validation and Integrated Multi-Physics Analysis of High-Speed Interior Permanent Magnet Synchronous Motor for Marine Exhaust Gas Recirculation Blower System

WonYoung Jo [1,2], DongHyeok Son [3] and YunHyun Cho [2,*]

[1] VGM Co., Ltd., Busan 44776, Republic of Korea; jo.wonyoung@vgm.co.kr
[2] Department of Electrical Engineering, Dong-A University, Busan 49315, Republic of Korea
[3] Sansystech Co., Ltd., Busan 46918, Republic of Korea; dhs@sansystech.co.kr
* Correspondence: yhcho@dau.ac.kr

Abstract

This study explores an integrated multi-physics design approach for a high-speed Interior Permanent Magnet Synchronous Motor (IPMSM) optimized for marine diesel engine Exhaust Gas Recirculation (EGR) blower systems. To satisfy the rigorous operational demands of marine environments, an IPMSM with a rated output of 150 kW and a base speed of 9000 rpm was developed. The design validity was rigorously verified through a comprehensive multi-physics framework using the Finite Element Method (FEM), ensuring a balance between electromagnetic, thermal, and mechanical performance. The investigation established a mathematical model for the IPMSM driven by a Space Vector Pulse-Width Modulation (SVPWM) inverter, facilitating a detailed analysis of steady-state characteristics within the EGR system. To guarantee long-term reliability at high rotational speeds, the study performed an integrated thermal analysis based on precise electrical loss separation and a rotor-dynamic evaluation focusing on unbalanced vibration responses of the shaft. Finally, the proposed design was validated by integrating the IPMSM into a full-scale EGR blower system. Experimental evaluations across the entire operating range confirm that the integrated design successfully achieves the high power density and mechanical robustness required for marine diesel applications.

Keywords: EGR blower system; high-speed IPMSM; integrated multi-physics design; thermal–structural coupled analysis

Check for updates

Academic Editor: Oscar Barambones

Received: 20 February 2026
Revised: 21 March 2026
Accepted: 22 March 2026
Published: 27 March 2026

Copyright: © 2026 by the authors. Licensee MDPI, Basel, Switzerland. This article is an open access article distributed under the terms and conditions of the Creative Commons Attribution (CC BY) license.

1. Introduction

With the stringent environmental regulations imposed by the International Maritime Organization (IMO), particularly the Tier III NOx emission limits, the adoption of Exhaust Gas Recirculation (EGR) systems in marine diesel engines has become indispensable [1–4]. The EGR blower, a pivotal component of this system, must reliably increase exhaust gas pressure to overcome scavenging air pressure under harsh maritime conditions. This operational context demands a drive motor with high power density, exceptional efficiency, and robust mechanical integrity to withstand high-speed rotation [5–8].

Interior Permanent Magnet Synchronous Motors (IPMSMs) are highly suitable for such high-speed applications, as they effectively utilize both magnetic and reluctance torque, providing superior performance over conventional induction motors [9–12]. However, increasing the operational speed to the 10,000 rpm range introduces complex multi-disciplinary challenges [13–16]. These include excessive centrifugal stress on the rotor ribs,

significant thermal escalation due to high-frequency iron and eddy current losses, and potential structural instability caused by critical speed resonance.

To address these interrelated issues, this study proposes a comprehensive and integrated multi-physics design framework. Unlike traditional sequential design methods, our approach concurrently evaluates electromagnetic, thermal, and rotor-dynamic characteristics to achieve an optimal balance. We present the development of a 150 kW, 9000 rpm IPMSM, specifically focusing on the optimization of the V-type rotor topology (Model 5) to maximize efficiency and mechanical safety. The validity of the proposed design is rigorously demonstrated through numerical simulations and further confirmed by experimental integration into a full-scale EGR blower system.

2. Electromagnetic Design and Rotor Topology Optimization

2.1. EGR Blower System and Required Specifications

Figure 1 shows the schematic diagram of the EGR blower system and IPMSM drive system for marine diesel engines. The EGR system consists of a main loop and an EGR blower system installed with an IPMSM and inverter. In the EGR main loop, clean air is injected into the engine through a compressor, an air cooler and the EGR blower system. The EGR blower system serves to keep the exhaust gas pressure lower than the scavenging air pressure [17]. To drive the impeller in the EGR blower, the motor drive system consists of an IPMSM and V/f inverter to control the speed of the motor. As shown in Figure 1, the required performance of the EGR blower system is a pressure ratio 1.04–1.2 and air flow 0.8–2.5 m^3/s, with a rated speed of 9000 rpm, while the rated power of the IPMSM is required to be 150 kW for a base speed of 9000 rpm. The input source is three-phase 380 V, 60 Hz and an inverter operating on a sensorless space vector PWM inverter with an LC filter [18–21].

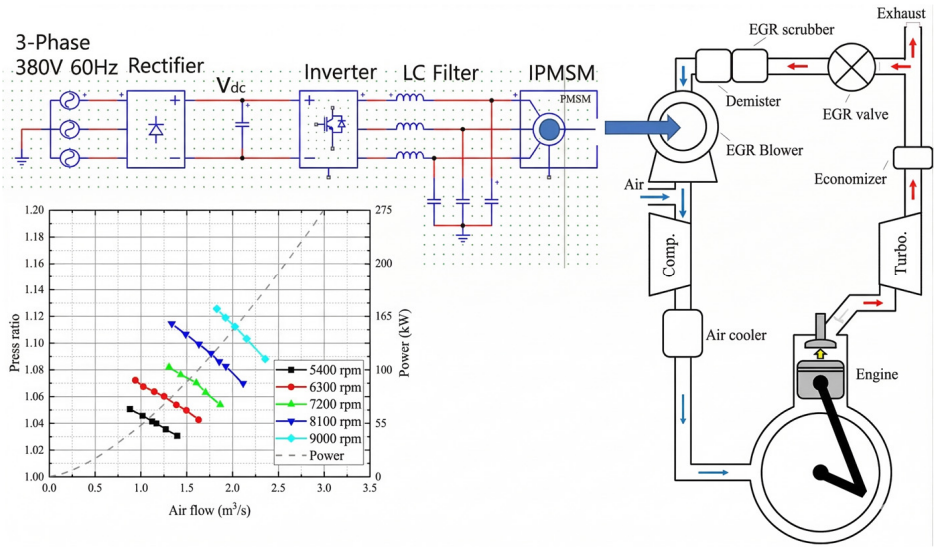
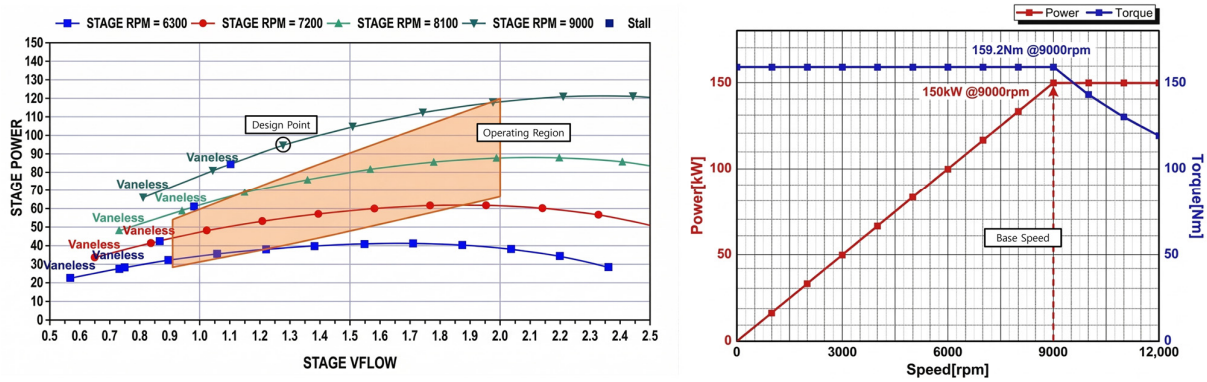


Figure 1. Schematic diagram of EGR blower system and its required performance.

Figure 2 shows the torque and output specification curves according to the speed of the motor of the EGR blower system under the flow rate and pressure ratio conditions. The motor's rotation speed is required to be designed to be at least 9000 rpm based on the blower speed and a maximum speed of 12,000 rpm. The space vector-type inverter must generate a maximum torque of 160 Nm and an output of 150 kW. The input DC link voltage of the inverter driving the IPMSM is set to 530 V. Table 1 shows the electrical specifications of the EGR blower system.



(**a**) (**b**)

Figure 2. Operational requirements for the 150 kW IPMSM. (**a**) Aerodynamic characteristic curves for various motor speeds; (**b**) torque and power vs. speed profiles.

Table 1. Motor specifications of EGR blower system.

Item	Value	Item	Value
rated power [kW]	150	Number of Poles [poles]	4
base speed [rpm]	9000	Number of Slots [slots]	36
rated torque [Nm]	160	Stator Outer Diameter [mm]	265
max. speed [rpm]	12,000	Rotor Outer Diameter [mm]	145
input voltage [V]	3-phase 380	Coil Diameter [mm]	Φ0.8 × 20 strands
inverter type	SV-PWM	Conductors per Slot [turns]	8
motor control	Sensorless (V/f)	Current Density [A_{peak}/mm^2]	5.9
motor efficiency [%]	≥96	PM Thickness × Width [mm]	Sm2Co17 20 × 9
max. temperature [°C]	≤150	Stator Core	20PNF1500
air gap length [mm]	1	Stack Length [mm]	200

2.2. Comparison of Rotor Topologies and Loss Analysis

To optimize the torque density and mechanical retention of the magnets, three rotor topologies were compared, as shown in Figure 3 [11]. The electromagnetic torque T_e is governed by:

$$T_e = \frac{3}{2}P[\psi_a i_q + (L_d - L_q) i_d i_q] \quad (1)$$

where P is the number of poles, ψ_a is the permanent magnet flux linkage, L_d and L_q are the d-axis and q-axis inductances, and i_d and i_q represent the stator current components. The first term represents the PM torque, while the second term denotes the reluctance torque arising from the inductance difference.

The V-type topology was selected because it provides the best balance between reluctance torque utilization and structural robustness at high speeds. Figure 3b illustrates the magnetic flux density distribution, where the flux density at the air gap level was carefully evaluated for each model. The results confirm that Model 5 achieves the most uniform distribution across the air gap by effectively managing magnetic saturation in the rotor ribs and bridges, thereby optimizing the torque density. The magnetic model and flux linkage maps were analyzed considering these saturation effects [14,15]. To refine the design, five iterations (Models 1–5) were evaluated by conducting a parametric sweep of the V-type barrier and bridge geometries. The key design variables included the magnet angle, center bridge thickness, and side rib thickness. As summarized in Table 2, Model 5 demonstrated the highest efficiency of 96.57%. The reduction in PM eddy current losses (from 610 W in Model 1 to 150 W in Model 5) highlights the effectiveness of the optimized barrier and bridge geometry.

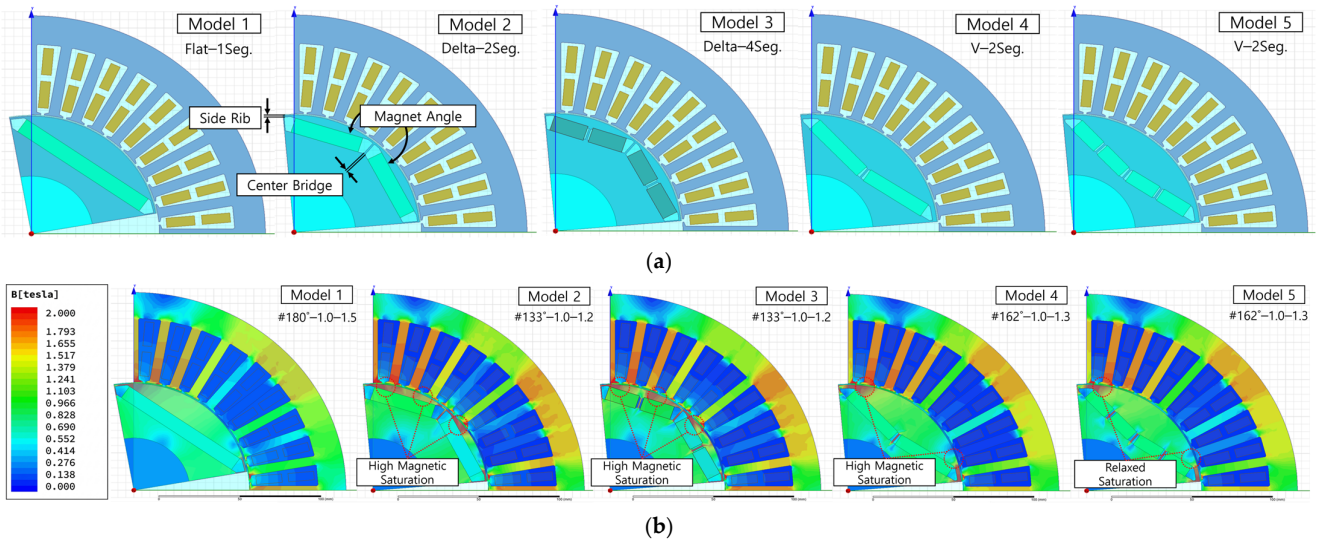


Figure 3. Electromagnetic FEM analysis results. (**a**) Comparison of rotor topologies (Flat, Delta and V-type); (**b**) magnetic flux density distribution analysis (# indicates magnet angle–center bridge–side rib).

Table 2. Performance and loss data comparison of the IPMSM at the rated power.

Item	Model 1	Model 2	Model 3	Model 4	Model 5
Average Torque [Nm]	159.5	159.2	159.4	159.3	159.0
Torque Ripple [%]	9.4	4.8	3.5	5.2	4.1
Iron Loss [W]	1710	1980	2100	1870	1890
Copper Loss [W]	2410	1680	1730	1790	1830
PM Eddy Current Loss [W]	610	390	130	410	150
Wind and friction loss [W]	1450	1450	1450	1450	1450
Total Loss [W]	6180	5500	5410	5520	5320
Efficiency [%]	96.04	96.46	96.52	96.45	96.57

To analyze the electromagnetic characteristics, a sensorless V/f control strategy based on SVPWM was employed. The voltage-to-frequency ratio was maintained at 1.2 to ensure constant torque within the base speed range. Table 2 provides a comparative analysis of electromagnetic losses and operational efficiency for the five design iterations (Models 1–5) at the rated power of 150 kW and 9000 rpm.

3. Integrated Multi-Physics Analysis

3.1. Multi-Physics Rotor-Dynamics and Strength Analysis

The proposed design employs an iterative multi-physics framework. Beyond simple sequential analysis, it incorporates a feedback loop where mechanical and thermal constraints are used to re-optimize electromagnetic parameters until all requirements are met concurrently.

3.1.1. Rotor-Dynamic Analysis

The dynamic stability of the rotor was verified using the following governing equation:

$$[M]\{\ddot{x}\} + ([C] + [G])\{\dot{x}\} + [K]\{x\} = \{F_{ext}\} \quad (2)$$

In this framework, M, C, and K denote the mass, damping, and stiffness matrices of the rotor-bearing system, respectively. The excitation force F_{ext} incorporates the Maxwell

stress distribution derived from the electromagnetic FEM analysis to predict unbalanced vibration responses.

The excitation force F_{ext} accounts for the Maxwell stress distribution derived from the electromagnetic FEM. Figure 4 visualizes the first bending mode, and Table 3 compares the simulated modal frequencies with experimental hammering test results. The measured first mode at 638.75 Hz (equivalent to 38,325 rpm) ensures a 325% separation margin from the rated speed, guaranteeing resonance-free operation.

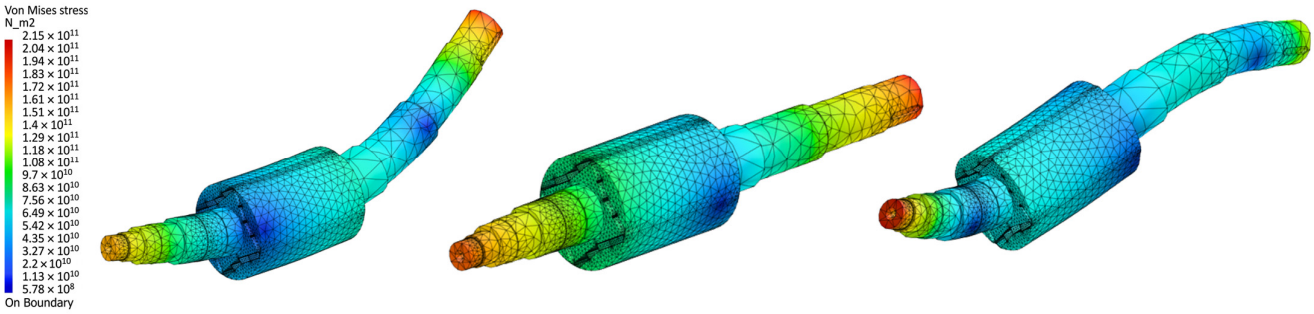


Figure 4. Predicted first bending mode shape of the Model 5 rotor assembly from the rotor-dynamic simulation (Model 5).

Table 3. Modal analysis and hammering test results for the rotor.

Mode Number	Simulated		Tested	
	Frequency [Hz]	Speed [rpm]	Frequency [Hz]	Speed [rpm]
1	662.99	39,779	638.75	38,325
2	664.01	39,840	644.01	38,640
3	1541.90	92,514	1523	91,380
4	1547.30	92,838	1547.30	92,838

3.1.2. Structural Strength Analysis

Mechanical safety at the maximum speed of 12,000 rpm was evaluated using the von Mises stress criteria. The analysis focuses on centrifugal stress at the rotor bridges and ribs, which are the most critical regions for structural integrity. The material properties of 20PNF1500 and Sm2Co17 used for the structural analysis are summarized in Table 4. Figure 5 shows that stress concentration occurs primarily at the magnet retention bridges. For Model 5, the peak stress of 227.0 MPa is well within the yield strength of the stator core material (410 MPa), resulting in a safety factor of 1.84. This confirms that Model 5 ensures mechanical reliability without permanent deformation at the maximum operational speed [22].

Table 4. Material properties for structural analysis.

Property	20PNF1500	Sm2Co17
Density [g/cm^3]	7.65	8.4
Young's modulus [MPa]	190,000	58,000
Poisson's ratio	0.30	0.26
Tensile yield strength [MPa]	410	5
Tensile ultimate strength [MPa]	495	42
Thermal conductivity [W/m·K]	26~28	10~13
Specific heat [J/kg·K]	469~490	350~380

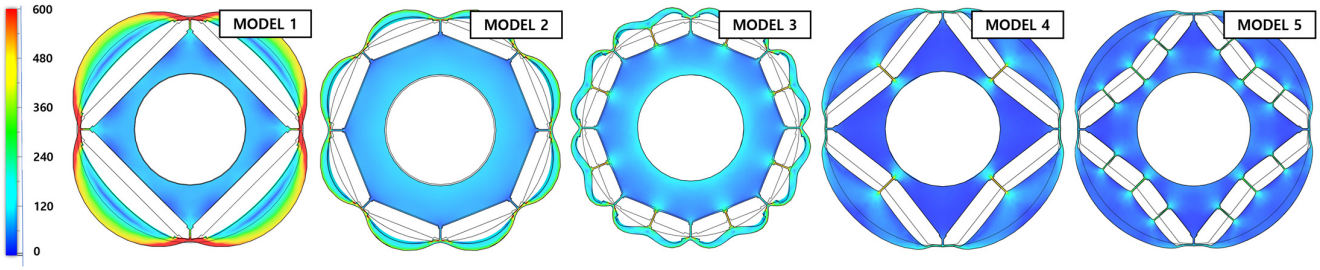


Figure 5. Equivalent von Mises stress distribution and mechanical safety evaluation of rotor candidates at the maximum operational speed of 12,000 rpm.

3.1.3. Selection of the Final Design (Model 5)

Based on the comparative analysis in Tables 2 and 5, Model 3 demonstrated the most superior mechanical integrity, with a minimum peak stress of 207.1 MPa and a safety factor of 1.98. However, Model 5 was ultimately selected as the final prototype, because it provides a more optimized balance between electromagnetic performance and practical manufacturability. While maintaining a sufficient safety factor of 1.84 at 12,000 rpm, Model 5 achieves the highest efficiency of 96.57% by maximizing reluctance torque utilization. Model 5 was selected over Model 3, not only for its superior efficiency (96.57%) but also for its lower manufacturing complexity and cost-effectiveness. While Model 3 has a higher safety factor (1.98), Model 5's safety factor of 1.84 sufficiently exceeds the 1.5 requirement while offering a more practical and economical V-type rotor geometry for mass production. Consequently, Model 5 was chosen for subsequent multi-physics thermal and rotor-dynamic evaluations.

Table 5. Safety factor calculation results via structural analysis.

Item	Model 1	Model 2	Model 3	Model 4	Model 5
Peak stress [MPa]	569.4	301.5	207.1	320.3	227.0
Safety factor	0.72	1.36	1.98	1.28	1.84

3.2. Multi-Physics Thermal Analysis

3.2.1. Loss Evaluation and Thermal Modeling

High-speed operation generates significant heat from iron losses and high-frequency harmonics. To ensure thermal stability, the calculated electrical losses (iron, copper, and eddy current losses) from Model 5 were mapped as volumetric heat sources, Q, into a 3D thermal FEM model:

$$\rho C_p \frac{\partial T}{\partial t} = \nabla \cdot (k \nabla T) + Q \quad (3)$$

Here, k is the thermal conductivity, and T is the local temperature. The bidirectional coupling is achieved by updating material properties (e.g., copper conductivity and magnet remanence) based on the calculated temperature, ensuring that the electromagnetic losses and thermal distribution reach a converged solution. This model accounts for the heat removal via the water_cooling jacket by applying forced convection boundary conditions.

The 3D thermal FEM was performed under specific cooling conditions to simulate the actual EGR environment. The cooling conditions (10 LPM, 35 °C) reflect standard marine engine room specifications. To ensure accurate thermal analysis, the forced convection heat transfer coefficient was computationally derived directly through the 3D thermal analysis software, SimScale (SimScale GmbH, Munich, Germany), cloud_based simulation platform. Specifically, the software calculated the coefficient based on the specific fluid properties (flow rate and inlet temperature) and the precise geometric dimensions (surface area

and channel volume) of the cooling jacket. This computationally derived coefficient was applied to the inner surface of the cooling jacket to ensure the accuracy of the steady-state temperature distribution [16,17].

3.2.2. Electromagnetic and Thermal Characteristics

Based on the loss separation analysis, the calculated electrical losses were applied as heat sources for the 3D thermal evaluation. Figure 6 shows the steady-state temperature distribution of the motor under continuous rated operation. Due to the integrated water_cooling jacket, the maximum temperature of the stator winding is stabilized at approximately 114 °C, and the Sm2Co17 permanent magnets remain below 150 °C. These results confirm a sufficient thermal safety margin against irreversible demagnetization, ensuring reliability in the high-temperature environments of marine engine rooms. To validate the proposed design, the performance and loss characteristics of Model 5 were compared with the measured data at rated power, and the results are summarized in Table 6.

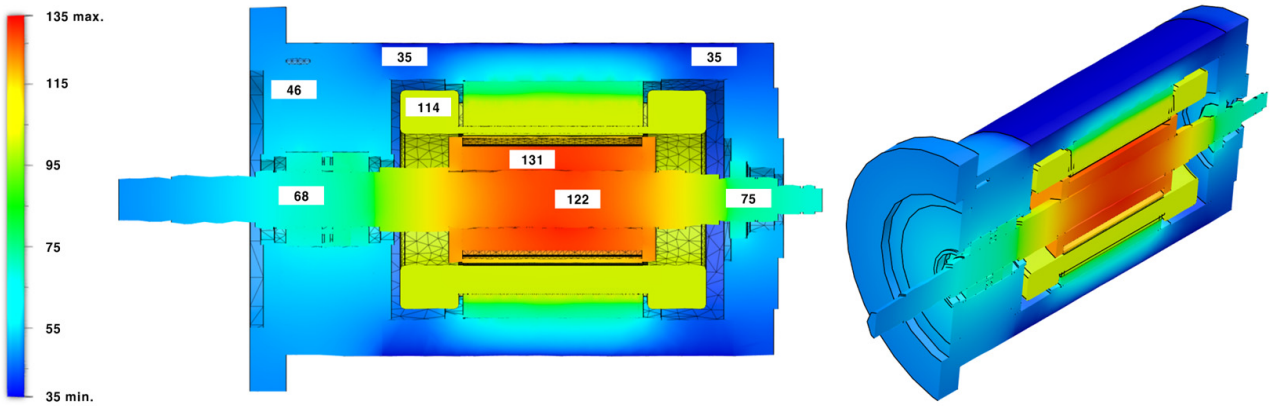


Figure 6. Predicted steady-state temperature distribution of the IPMSM under continuous rated load (150 kW, 9000 rpm) with active water cooling.

Table 6. Comparison of performance and loss data for Model 5 at rated power (total iron loss, comprising hysteresis and eddy current loss).

Item	Simulated	Measured	Item	Simulated	Measured
Line Voltage [V]	3Φ-380	3Φ-380	Iron Loss [W]	2040	1910
Current [A]	241.8	241.0	Copper Loss [W]	1830	1795
Input Power [kW]	155.2	155.24	Wind and Friction [W]	1450	1445
Motor Speed [rpm]	9000	9000	Total Loss [W]	5320	5150
Motor Torque [Nm]	159.0	159.28	Motor Effi. [%]	96.57	96.68
Output Power [kW]	149.9	150.12	Motor PF [%]	97.5	97.8

4. Experimental Validation for Model 5

4.1. Experimental Results

The final prototype (Model 5) was validated using the experimental setup shown in Figure 7. The measurement results (presented in Figure 8) demonstrate a high degree of correlation with the initial design predictions.

Specifically, Figure 8a,b shows that the measured no-load Back-EMF aligns closely with the FEM results, showing only a 1.2% error. The operational performance curves in Figure 8c and the temperature saturation curves in Figure 8d further confirm the accuracy of the multi-physics analysis. Under continuous rated operation, the motor reached a stable efficiency of 96.68%, proving that the proposed integrated design framework effectively

ensures the reliability and high-power density required for marine EGR blower systems. It is worth noting that the measured total loss (5150 W) was slightly lower than the initial simulation (5320 W). This discrepancy may arise from the conservative estimation of windage and friction losses in the FEM model, which were found to be approximately 170 W lower in the actual experimental environment.

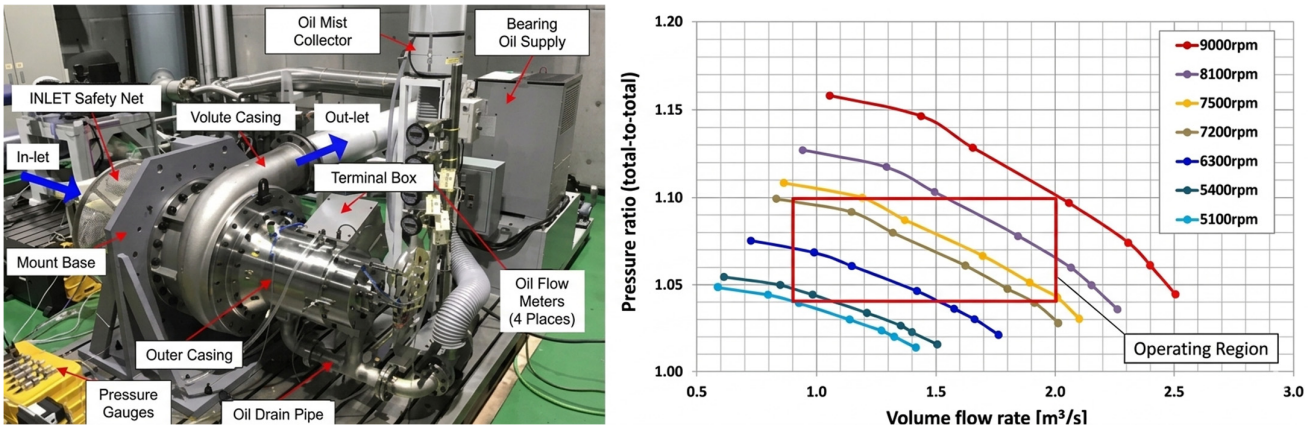


Figure 7. Experimental setup for EGR blower system with final Model 5.

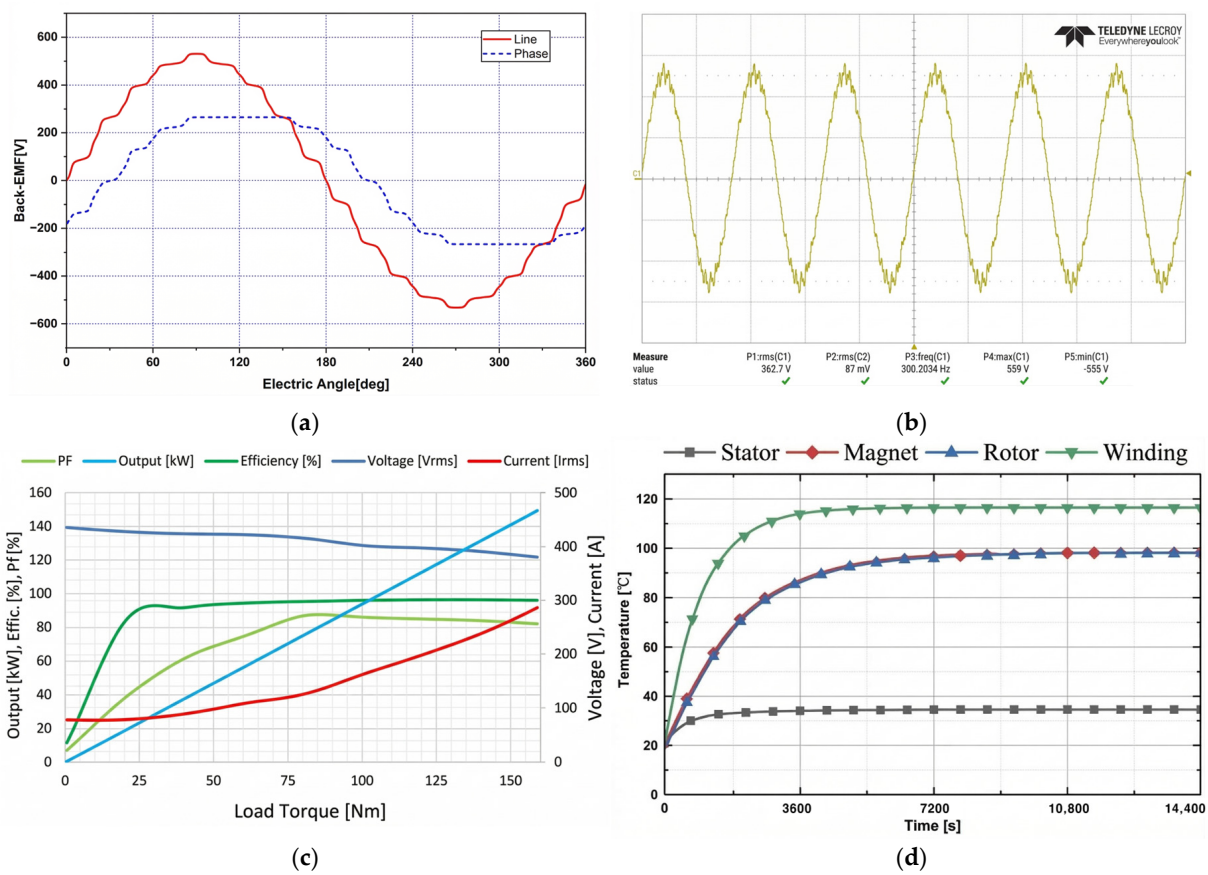


Figure 8. Experimental validation results for Model 5. (**a**) B-EMF simulated result; (**b**) B-EMF measured result (scale: 200 V/div, 2 ms/div); (**c**) performance curves; (**d**) temperature saturation curves.

4.2. Discussion of the Integrated Design Approach

The integration of multi-physics analysis in the early design stage is crucial for high-speed marine applications. Traditional design methods often treat electromagnetic and mechanical constraints separately, which can lead to thermal failure or resonance issues

during actual operation. In this study, the V-type rotor topology was selected not only for its high saliency ratio but also for its structural robustness.

One key observation during the experimental validation was the slight deviation in iron loss compared to the initial FEM predictions. This is attributed to the manufacturing processes, such as the shrink-fitting of the cooling jacket and the high-frequency harmonics generated by the SVPWM inverter. Despite these factors, the proposed integrated framework successfully predicted the thermal saturation within a 5% error margin, proving its efficacy as a reliable design tool for high-power density marine motors.

5. Conclusions

This paper presented an integrated multi-physics design and experimental validation of a 150 kW, 9000 rpm IPMSM for marine diesel engine EGR blower systems. The research yielded several significant conclusions:

1. Topology Optimization and Selection of Model 5: While Model 3 exhibited the highest structural safety factor, Model 5 was chosen as the superior design, as it achieved the highest efficiency of 96.68%. This was made possible by optimizing the V-type barrier geometry to maximize the saliency ratio and reluctance torque utilization while maintaining a robust safety factor of 1.84.
2. Reliability Verification via Multi-physics Coupling: The sequential coupled analysis confirmed both structural and thermal integrity. Iterative optimization of the rotor bridge in Model 5 successfully reduced the peak stress to 227.0 MPa, ensuring a safety factor of 1.84. Simultaneously, the 3D thermal analysis verified that the Sm2Co17 magnets remain below 150 °C, providing a sufficient margin against demagnetization.
3. System Validation: The final prototype (Model 5) achieved a maximum efficiency of 96.68% in experimental tests. When integrated into the EGR blower system, it demonstrated superior efficiency compared to conventional induction motor systems that are generally used in marine applications, confirming its suitability for energy-saving objectives.

The proposed integrated design framework provides a robust and systematic methodology for developing high-performance electric machines for harsh marine environments. Future work will focus on further optimizing the sensorless control algorithms to enhance the system's dynamic response under transient load conditions.

Author Contributions: Conceptualization, W.J., D.S. and Y.C.; methodology, software W.J.; validation, W.J., D.S. and Y.C.; formal analysis, investigation, writing—original draft preparation, W.J.; writing—review and editing, Y.C.; visualization, W.J.; supervision, Y.C. All authors have read and agreed to the published version of the manuscript.

Funding: This research received no external funding.

Institutional Review Board Statement: Not applicable.

Informed Consent Statement: Not applicable.

Data Availability Statement: The original contributions presented in this study are included in the article. Further inquiries can be directed to the corresponding author.

Acknowledgments: This research was supported by the Dong-A University research fund.

Conflicts of Interest: Authors W.J. and D.S. was employed by the VGM Co., Ltd. and Sansystech Co., Ltd., respectively. The remaining author declares that the research was conducted in the absence of any commercial or financial relationships that could be construed as a potential conflict of interest.

References

1. Zhao, W.; Chen, D.; Lipo, T.A.; Kwon, B.I. Optimal Design of a High-Speed Interior Permanent Magnet Synchronous Machine for EV Applications. *IEEE Trans. Magn.* **2014**, *50*, 1–4.
2. Li, W.; Cheng, S.; Zhang, C.; Gao, P. Multi-Physics Integrated Design of a High-Speed Interior Permanent Magnet Motor. *IEEE Trans. Ind. Electron.* **2021**, *68*, 5581–5591.
3. Valente, G.; Papini, L.; Formentini, A.; Gerada, C.; Zanchetta, P. Multi-physics Design Optimization of High-Speed Permanent Magnet Machines. *IEEE Trans. Ind. Electron.* **2017**, *64*, 9762–9771.
4. Yan, F.; Wang, Y.; Li, J.; Cheng, Q. Research of Post Injection Strategy of an EGR Diesel Engine to Improve Combustion and Particulate Emissions Performance: Application on the Transient Operation. *Symmetry* **2020**, *12*, 2002. [CrossRef]
5. Zhang, G.; Hua, W.; Cheng, M.; Liao, K.; Wang, J. Multi-physics Design and Analysis of a High-Speed Interior Permanent Magnet Machine for Electric Vehicles. *Energies* **2019**, *12*, 2841.
6. Kim, S.-A. A Study on the Predictive Maintenance Algorithms Considering Load Characteristics of PMSMs to Drive EGR Blowers for Smart Ships. *Energies* **2021**, *14*, 5744. [CrossRef]
7. Zhang, H.; Wang, X.; Chen, L.; Zhao, J. Effects of Different Exhaust Gas Recirculation (EGR) Rates on Combustion and Emission Characteristics of Biodiesel–Diesel Blended Fuel Based on an Improved Chemical Mechanism. *Energies* **2022**, *15*, 4153. [CrossRef]
8. Liu, Z.; Zhang, Y.; Li, S. Research and Analysis of Explosion-Proof Diesel Engine Performance Based on Different Exhaust Gas Cooling Systems. *Energies* **2025**, *18*, 610. [CrossRef]
9. Li, W.; Cheng, S.; Zhang, C.; Gao, P. Mechanical Analysis and Design of a High-Speed Interior Permanent Magnet Rotor. *IEEE Trans. Magn.* **2018**, *54*, 1–5.
10. Kim, S.-A.; Hong, K.-P. Analysis and Experimental Verification of a Variable Speed Turbo Air Centrifugal Compressor System for Energy Saving. *Energies* **2021**, *14*, 1208. [CrossRef]
11. Popa, M.G.; Iorga, D.; Burnete, N. Impact of Heat Exchanger Effectiveness and EGR on Energy and Emission Performance of a CI Engine. *Appl. Sci.* **2025**, *15*, 8780. [CrossRef]
12. He, X.; Zhang, Q.; Zhao, R. Numerical Optimization of the EGR Rate and Injection Timing with a Novel Cavitation Model in a Diesel Engine Fueled with PODE/Diesel Blends. *Appl. Sci.* **2022**, *12*, 24456. [CrossRef]
13. Kim, M.-S.; Kim, S.-A. Design and Experimental Verification of Hubless Rim-Driven Propulsor Consisting of Bearingless Propeller for an Unmanned Underwater Drone. *Energies* **2023**, *16*, 7458. [CrossRef]
14. Tan, Y.; Feng, L.; Lin, Q.; Guo, J.; Liang, X. Design of an Optimum Compact EGR Cooler in a Heavy-Duty Diesel Engine towards Meeting Euro 7 Emission Regulations. *Sustainability* **2023**, *15*, 12361. [CrossRef]
15. Nguyen, T.X.; Hoang, A.T. Combustion and Emission Trade-Offs in Tier-Regulated EGR Modes: Comparative Insights from Shop and Sea Operation Data of a CPP Marine Diesel Engine. *J. Mar. Sci. Eng.* **2025**, *13*, 1935. [CrossRef]
16. Choi, J.-H.; Kim, S.-W.; Park, S. Study on the Effects of Exhaust Gas Recirculation and Fuel Injection Strategy on Transient Process Performance of Diesel Engines. *Sustainability* **2023**, *15*, 12403. [CrossRef]
17. Yamazaki, K.; Watari, N. Loss Analysis of Permanent Magnet Motors Using Combination of 2-D and 3-D Finite Element Method. *IEEE Trans. Magn.* **2005**, *41*, 1980–1983. [CrossRef]
18. Ge, J.; Hu, Y.; Geng, H. Research on the High-Speed IPMSM for Marine Blower Applications. *J. Mar. Sci. Eng.* **2020**, *8*, 452.
19. Boglietti, A.; Cavagnino, A.; Staton, D.; Shanel, M.; Mueller, M.; Mejuto, C. Evolution and Modern Approaches for Thermal Analysis of Electrical Machines. *IEEE Trans. Ind. Electron.* **2009**, *56*, 871–882. [CrossRef]
20. Hariganesh, R.; Pugazhendhi, A.; Alagumalai, A. Influence of EGR and Acoustic Waves on Particles and Other Emissions of IC Engine Powered with Diesel and RME Fuels. *Stats* **2025**, *6*, 67.
21. Lewandowksi, M.; Sroka, Z.J. Impact of Multi-Valve Exhaust Gas Recirculation (EGR) System on Nitrogen Oxides Emissions in a Multi-Cylinder Engine. *Energies* **2024**, *17*, 6473.
22. Kuiken, K. *Diesel Engines for Ship Propulsion and Power Plants*; Target Global Energy Training: Onnen, The Netherlands, 2012; Volume 2.

Disclaimer/Publisher's Note: The statements, opinions and data contained in all publications are solely those of the individual author(s) and contributor(s) and not of MDPI and/or the editor(s). MDPI and/or the editor(s) disclaim responsibility for any injury to people or property resulting from any ideas, methods, instructions or products referred to in the content.